

First cross-correlation analysis of interferometric and resonant-bar gravitational-wave data for stochastic backgrounds

B. Abbott,¹⁴ R. Abbott,¹⁴ R. Adhikari,¹⁴ J. Agresti,¹⁴ P. Ajith,² B. Allen,^{2,51} R. Amin,¹⁸ S. B. Anderson,¹⁴ W. G. Anderson,⁵¹ M. Arain,³⁹ M. Araya,¹⁴ H. Armandula,¹⁴ M. Ashley,⁴ S. Aston,³⁸ P. Aufmuth,³⁵ C. Aulbert,¹ S. Babak,¹ S. Ballmer,¹⁴ H. Bantilan,⁸ B. C. Barish,¹⁴ C. Barker,¹⁶ D. Barker,¹⁶ B. Barr,⁴⁰ P. Barriga,⁵⁰ M. A. Barton,⁴⁰ K. Bayer,¹⁵ K. Belczynski,²⁴ J. Betzwieser,¹⁵ P. T. Beyersdorf,²⁷ B. Bhawal,¹⁴ I. A. Bilenko,²¹ G. Billingsley,¹⁴ R. Biswas,⁵¹ E. Black,¹⁴ K. Blackburn,¹⁴ L. Blackburn,¹⁵ D. Blair,⁵⁰ B. Bland,¹⁶ J. Bogenstahl,⁴⁰ L. Bogue,¹⁷ R. Bork,¹⁴ V. Boschi,¹⁴ S. Bose,⁵² P. R. Brady,⁵¹ V. B. Braginsky,²¹ J. E. Brau,⁴³ M. Brinkmann,² A. Brooks,³⁷ D. A. Brown,^{14,6} A. Bullington,³⁰ A. Bunkowski,² A. Buonanno,⁴¹ M. Burgamy,^{18,*} O. Burmeister,² D. Busby,^{14,†} R. L. Byer,³⁰ L. Cadonati,¹⁵ G. Cagnoli,⁴⁰ J. B. Camp,²² J. Cannizzo,²² K. Cannon,⁵¹ C. A. Cantley,⁴⁰ J. Cao,¹⁵ L. Cardenas,¹⁴ M. M. Casey,⁴⁰ G. Castaldi,⁴⁶ C. Cepeda,¹⁴ E. Chalkey,⁴⁰ P. Charlton,⁹ S. Chatterji,¹⁴ S. Chelkowski,² Y. Chen,¹ F. Chiadini,⁴⁵ D. Chin,⁴² E. Chin,⁵⁰ J. Chow,⁴ N. Christensen,⁸ J. Clark,⁴⁰ P. Cochrane,² T. Cokelaer,⁷ C. N. Colacino,³⁸ R. Coldwell,³⁹ R. Conte,⁴⁵ D. Cook,¹⁶ T. Corbitt,¹⁵ D. Coward,⁵⁰ D. Coyne,¹⁴ J. D. E. Creighton,⁵¹ T. D. Creighton,¹⁴ R. P. Croce,⁴⁶ D. R. M. Crooks,⁴⁰ A. M. Cruise,³⁸ A. Cumming,⁴⁰ J. Dalrymple,³¹ E. D'Ambrosio,¹⁴ K. Danzmann,^{2,35} G. Davies,⁷ D. DeBra,³⁰ J. Degallaix,⁵⁰ M. Degree,³⁰ T. Demma,⁴⁶ V. Dergachev,⁴² S. Desai,³² R. DeSalvo,¹⁴ S. Dhurandhar,¹³ M. Díaz,³³ J. Dickson,⁴ A. Di Credico,³¹ G. Diederichs,³⁵ A. Dietz,⁷ E. E. Doomes,²⁹ R. W. P. Drever,⁵ J.-C. Dumas,⁵⁰ R. J. Dupuis,¹⁴ J. G. Dwyer,¹⁰ P. Ehrens,¹⁴ E. Espinoza,¹⁴ T. Etzel,¹⁴ M. Evans,¹⁴ T. Evans,¹⁷ S. Fairhurst,^{7,14} Y. Fan,⁵⁰ D. Fazi,¹⁴ M. M. Fejer,³⁰ L. S. Finn,³² V. Fiumara,⁴⁵ N. Fotopoulos,⁵¹ A. Franzen,³⁵ K. Y. Franzen,³⁹ A. Freise,³⁸ R. Frey,⁴³ T. Fricke,⁴⁴ P. Fritschel,¹⁵ V. V. Frolov,¹⁷ M. Fyffe,¹⁷ V. Galdi,⁴⁶ J. Garofoli,¹⁶ I. Gholami,¹ J. A. Giaime,^{17,18} S. Giampanis,⁴⁴ K. D. Giardina,¹⁷ K. Goda,¹⁵ E. Goetz,⁴² L. Goggin,¹⁴ G. González,¹⁸ S. Gossler,⁴ A. Grant,⁴⁰ S. Gras,⁵⁰ C. Gray,¹⁶ M. Gray,⁴ J. Greenhalgh,²⁶ A. M. Gretarsson,¹¹ R. Grosso,³³ H. Grote,² S. Grunewald,¹ M. Guenther,¹⁶ R. Gustafson,⁴² B. Hage,³⁵ W. O. Hamilton,^{18,*} D. Hammer,⁵¹ C. Hanna,¹⁸ J. Hanson,^{17,†} J. Harms,² G. Harry,^{15,†} E. Harstad,⁴³ T. Hayler,²⁶ J. Heefner,¹⁴ I. S. Heng,^{40,†} A. Heptonstall,⁴⁰ M. Heurs,² M. Hewitson,² S. Hild,³⁵ E. Hirose,³¹ D. Hoak,¹⁷ D. Hosken,³⁷ J. Hough,⁴⁰ E. Howell,⁵⁰ D. Hoyland,³⁸ S. H. Huttner,⁴⁰ D. Ingram,¹⁶ E. Innerhofer,¹⁵ M. Ito,⁴³ Y. Itoh,⁵¹ A. Ivanov,¹⁴ D. Jackrel,³⁰ B. Johnson,¹⁶ W. W. Johnson,^{18,†} D. I. Jones,⁴⁷ G. Jones,⁷ R. Jones,⁴⁰ L. Ju,⁵⁰ P. Kalmus,¹⁰ V. Kalogera,²⁴ D. Kasprzyk,³⁸ E. Katsavounidis,¹⁵ K. Kawabe,¹⁶ S. Kawamura,²³ F. Kawazoe,²³ W. Kells,¹⁴ D. G. Keppel,¹⁴ F. Ya. Khalili,²¹ C. Kim,²⁴ P. King,¹⁴ J. S. Kissel,¹⁸ S. Klimenko,³⁹ K. Kokeyama,²³ V. Kondrashov,¹⁴ R. K. Kopparapu,¹⁸ D. Kozak,¹⁴ B. Krishnan,¹ P. Kwee,³⁵ P. K. Lam,⁴ M. Landry,¹⁶ B. Lantz,³⁰ A. Lazzarini,¹⁴ B. Lee,⁵⁰ M. Lei,¹⁴ J. Leiner,⁵² V. Leonhardt,²³ I. Leonor,⁴³ K. Libbrecht,¹⁴ P. Lindquist,¹⁴ N. A. Lockerbie,⁴⁸ M. Longo,⁴⁵ M. Lormand,¹⁷ M. Lubinski,¹⁶ H. Lück,^{2,35} B. Machenschalk,¹ M. MacInnis,¹⁵ M. Mageswaran,¹⁴ K. Maitland,¹⁴ M. Malec,³⁵ V. Mandic,¹⁴ S. Marano,⁴⁵ S. Márka,¹⁰ J. Markowitz,¹⁵ E. Maros,¹⁴ I. Martin,⁴⁰ J. N. Marx,¹⁴ K. Mason,¹⁵ L. Matone,¹⁰ V. Matta,⁴⁵ N. Mavalvala,¹⁵ R. McCarthy,¹⁶ B. J. McCauley,²⁰ D. E. McClelland,⁴ S. C. McGuire,²⁹ M. McHugh,^{20,†} K. McKenzie,⁴ J. W. C. McNabb,³² S. McWilliams,²² T. Meier,³⁵ A. Melissinos,⁴⁴ G. Mendell,¹⁶ R. A. Mercer,³⁹ S. Meshkov,¹⁴ E. Messaritaki,¹⁴ C. J. Messenger,⁴⁰ D. Meyers,¹⁴ E. Mikhailov,¹⁵ P. Miller,^{18,*} S. Mitra,¹³ V. P. Mitrofanov,²¹ G. Mitselmakher,³⁹ R. Mittleman,¹⁵ O. Miyakawa,¹⁴ S. Mohanty,³³ V. Moody,^{41,*} G. Moreno,¹⁶ K. Mossavi,² C. MowLowry,⁴ A. Moylan,⁴ D. Mudge,³⁷ G. Mueller,³⁹ S. Mukherjee,³³ H. Müller-Ebhardt,² J. Munch,³⁷ P. Murray,⁴⁰ E. Myers,¹⁶ J. Myers,¹⁶ T. Nash,¹⁴ D. Nettle,^{18,*} G. Newton,⁴⁰ A. Nishizawa,²³ K. Numata,²² B. O'Reilly,¹⁷ R. O'Shaughnessy,²⁴ D. J. Ottaway,¹⁵ H. Overmire,¹⁷ B. J. Owen,³² H.-J. Paik,^{41,*} Y. Pan,⁴¹ M. A. Papa,^{1,51} V. Parameshwaraiah,¹⁶ P. Patel,¹⁴ M. Pedraza,¹⁴ S. Penn,¹² V. Pierro,⁴⁶ I. M. Pinto,⁴⁶ M. Pitkin,⁴⁰ H. Pletsch,⁵¹ M. V. Plissi,⁴⁰ F. Postiglione,⁴⁵ R. Prix,¹ V. Quetschke,³⁹ F. Raab,¹⁶ D. Rabeling,⁴ H. Radkins,¹⁶ R. Rahkola,⁴³ N. Rainer,² M. Rakhmanov,³² M. Ramsunder,³² K. Rawlins,¹⁷ S. Ray-Majumder,⁵¹ V. Re,³⁸ H. Rehbein,² S. Reid,⁴⁰ D. H. Reitze,³⁹ L. Ribichini,² R. Riesen,¹⁷ K. Riles,⁴² B. Rivera,¹⁶ N. A. Robertson,^{14,40} C. Robinson,⁷ E. L. Robinson,³⁸ S. Roddy,¹⁷ A. Rodriguez,¹⁸ A. M. Rogan,⁵² J. Rollins,¹⁰ J. D. Romano,⁷ J. Romie,¹⁷ R. Route,³⁰ S. Rowan,⁴⁰ A. Rüdiger,² L. Ruet,¹⁵ P. Russell,¹⁴ K. Ryan,¹⁶ S. Sakata,²³ M. Samidi,¹⁴ L. Sancho de la Jordana,³⁶ V. Sandberg,¹⁶ V. Sannibale,¹⁴ S. Saraf,²⁵ P. Sarin,¹⁵ B. S. Sathyaprakash,⁷ S. Sato,²³ P. R. Saulson,³¹ R. Savage,¹⁶ P. Savov,⁶ S. Schediwy,⁵⁰ R. Schilling,² R. Schnabel,² R. Schofield,⁴³ B. F. Schutz,^{1,7} P. Schwinberg,¹⁶ S. M. Scott,⁴ A. C. Searle,⁴ B. Sears,¹⁴ F. Seifert,² D. Sellers,¹⁷ A. S. Sengupta,⁷ P. Shawhan,⁴¹ D. H. Shoemaker,¹⁵ A. Sibley,¹⁷ J. A. Sidles,⁴⁹ X. Siemens,^{6,14} D. Sigg,¹⁶ S. Sinha,³⁰ A. M. Sintes,^{1,36} B. J. J. Slagmolen,⁴ J. Slutsky,¹⁸ J. R. Smith,² M. R. Smith,¹⁴ K. Somiya,^{1,2} K. A. Strain,⁴⁰ D. M. Strom,⁴³ A. Stuver,³² T. Z. Summerscales,³ K.-X. Sun,³⁰ M. Sung,¹⁸ P. J. Sutton,¹⁴ H. Takahashi,¹ D. B. Tanner,³⁹ M. Tarallo,¹⁴ R. Taylor,¹⁴ R. Taylor,⁴⁰ J. Thacker,¹⁷ K. A. Thorne,³² K. S. Thorne,⁶ A. Thüring,³⁵ K. V. Tokmakov,⁴⁰

C. Torres,³³ C. Torrie,⁴⁰ G. Traylor,¹⁷ M. Trias,³⁶ W. Tyler,¹⁴ D. Ugolini,³⁴ C. Ungarelli,³⁸ K. Urbanek,³⁰ H. Vahlbruch,³⁵ M. Vallisneri,⁶ C. Van Den Broeck,⁷ M. Varvella,¹⁴ S. Vass,¹⁴ A. Vecchio,³⁸ J. Veitch,⁴⁰ P. Veitch,³⁷ A. Villar,¹⁴ C. Vorvick,¹⁶ S. P. Vyachanin,²¹ S. J. Waldman,¹⁴ L. Wallace,¹⁴ H. Ward,⁴⁰ R. Ward,¹⁴ K. Watts,¹⁷ J. Weaver,^{18,*} D. Webber,¹⁴ A. Weber,^{18,*} A. Weidner,² M. Weinert,² A. Weinstein,¹⁴ R. Weiss,¹⁵ S. Wen,¹⁸ K. Wette,⁴ J. T. Whelan,¹ D. M. Whitbeck,³² S. E. Whitcomb,¹⁴ B. F. Whiting,³⁹ C. Wilkinson,¹⁶ P. A. Willems,¹⁴ L. Williams,³⁹ B. Willke,^{2,35} I. Wilmot,²⁶ W. Winkler,² C. C. Wipf,¹⁵ S. Wise,³⁹ A. G. Wiseman,⁵¹ G. Woan,⁴⁰ D. Woods,⁵¹ R. Wooley,¹⁷ J. Worden,¹⁶ W. Wu,³⁹ I. Yakushin,¹⁷ H. Yamamoto,¹⁴ Z. Yan,⁵⁰ S. Yoshida,²⁸ N. Yunes,³² M. Zanolin,¹⁵ J. Zhang,⁴² L. Zhang,¹⁴ P. Zhang,^{18,*} C. Zhao,⁵⁰ N. Zotov,¹⁹ M. Zucker,¹⁵ H. zur Mühlen,³⁵ and J. Zweizig¹⁴

(LIGO Scientific Collaboration and ALLEGRO Collaboration)[‡]

¹*Albert-Einstein-Institut, Max-Planck-Institut für Gravitationsphysik, D-14476 Golm, Germany*

²*Albert-Einstein-Institut, Max-Planck-Institut für Gravitationsphysik, D-30167 Hannover, Germany*

³*Andrews University, Berrien Springs, Michigan 49104, USA*

⁴*Australian National University, Canberra, 0200, Australia*

⁵*California Institute of Technology, Pasadena, California 91125, USA*

⁶*Caltech-CaRT, Pasadena, California 91125, USA*

⁷*Cardiff University, Cardiff, CF24 3AA, United Kingdom*

⁸*Carleton College, Northfield, Minnesota 55057, USA*

⁹*Charles Sturt University, Wagga Wagga, NSW 2678, Australia*

¹⁰*Columbia University, New York, New York 10027, USA*

¹¹*Embry-Riddle Aeronautical University, Prescott, Arizona 86301, USA*

¹²*Hobart and William Smith Colleges, Geneva, New York 14456, USA*

¹³*Inter-University Centre for Astronomy and Astrophysics, Pune-411007, India*

¹⁴*LIGO-California Institute of Technology, Pasadena, California 91125, USA*

¹⁵*LIGO Hanford Observatory, Richland, Washington 99352, USA*

¹⁶*LIGO Livingston Observatory, Livingston, Louisiana 70754, USA*

¹⁷*LIGO-Massachusetts Institute of Technology, Cambridge, Massachusetts 02139, USA*

¹⁸*Louisiana State University, Baton Rouge, Louisiana 70803, USA*

¹⁹*Louisiana Tech University, Ruston, Louisiana 71272, USA*

²⁰*Loyola University, New Orleans, Louisiana 70118, USA*

²¹*Moscow State University, Moscow, 119992, Russia*

²²*NASA/Goddard Space Flight Center, Greenbelt, Maryland 20771, USA*

²³*National Astronomical Observatory of Japan, Tokyo 181-8588, Japan*

²⁴*Northwestern University, Evanston, Illinois 60208, USA*

²⁵*Rochester Institute of Technology, Rochester, New York 14623, USA*

²⁶*Rutherford Appleton Laboratory, Chilton, Didcot, Oxon OX11 0QX United Kingdom*

²⁷*San Jose State University, San Jose, California 95192, USA*

²⁸*Southeastern Louisiana University, Hammond, Louisiana 70402, USA*

²⁹*Southern University and A&M College, Baton Rouge, Louisiana 70813, USA*

³⁰*Stanford University, Stanford, California 94305, USA*

³¹*Syracuse University, Syracuse, New York 13244, USA*

³²*The Pennsylvania State University, University Park, Pennsylvania 16802, USA*

³³*The University of Texas at Brownsville and Texas Southmost College, Brownsville, Texas 78520, USA*

³⁴*Trinity University, San Antonio, Texas 78212, USA*

³⁵*Universitat de les Illes Balears, E-07122 Palma de Mallorca, Spain*

³⁶*Universität Hannover, D-30167 Hannover, Germany*

³⁷*University of Adelaide, Adelaide, SA 5005, Australia*

³⁸*University of Birmingham, Birmingham, B15 2TT, United Kingdom*

³⁹*University of Florida, Gainesville, Florida 32611, USA*

⁴⁰*University of Glasgow, Glasgow, G12 8QQ, United Kingdom*

⁴¹*University of Maryland, College Park, Maryland 20742 USA*

⁴²*University of Michigan, Ann Arbor, Michigan 48109, USA*

⁴³*University of Oregon, Eugene, Oregon 97403, USA*

⁴⁴*University of Rochester, Rochester, New York 14627, USA*

⁴⁵*University of Salerno, 84084 Fisciano (Salerno), Italy*

⁴⁶*University of Sannio at Benevento, I-82100 Benevento, Italy*

⁴⁷*University of Southampton, Southampton, SO17 1BJ, United Kingdom*

⁴⁸*University of Strathclyde, Glasgow, G1 1XQ, United Kingdom*

⁴⁹*University of Washington, Seattle, Washington 98195, USA*⁵⁰*University of Western Australia, Crawley, Washington 6009, Australia, USA*⁵¹*University of Wisconsin-Milwaukee, Milwaukee, Wisconsin 53201, USA*⁵²*Washington State University, Pullman, Washington 99164, USA*

(Received 28 March 2007; published 9 July 2007)

Data from the LIGO Livingston interferometer and the ALLEGRO resonant-bar detector, taken during LIGO's fourth science run, were examined for cross correlations indicative of a stochastic gravitational-wave background in the frequency range 850–950 Hz, with most of the sensitivity arising between 905 and 925 Hz. ALLEGRO was operated in three different orientations during the experiment to modulate the relative sign of gravitational-wave and environmental correlations. No statistically significant correlations were seen in any of the orientations, and the results were used to set a Bayesian 90% confidence level upper limit of $\Omega_{\text{gw}}(f) \leq 1.02$, which corresponds to a gravitational-wave strain at 915 Hz of $1.5 \times 10^{-23} \text{ Hz}^{-1/2}$. In the traditional units of $h_{100}^2 \Omega_{\text{gw}}(f)$, this is a limit of 0.53, 2 orders of magnitude better than the previous direct limit at these frequencies. The method was also validated with successful extraction of simulated signals injected in hardware and software.

DOI: [10.1103/PhysRevD.76.022001](https://doi.org/10.1103/PhysRevD.76.022001)

PACS numbers: 04.80.Nn, 04.30.Db, 07.05.Kf, 95.55.Ym

I. INTRODUCTION

One of the signals targeted by the current generation of ground-based gravitational-wave (GW) detectors is a stochastic gravitational-wave background (SGWB) [1–3]. Such a background is analogous to the cosmic microwave background, although the dominant contribution is unlikely to have a blackbody spectrum. A SGWB can be characterized as cosmological or astrophysical in origin. Cosmological backgrounds can arise from, for example, pre-big-bang models [4–6], amplification of quantum vacuum fluctuations during inflation [7–9], phase transitions [10,11], and cosmic strings [12–14]. Astrophysical backgrounds consist of a superposition of unresolved sources, which can include rotating neutron stars [15,16], supernovae [17], and low-mass x-ray binaries [18].

The standard cross-correlation search [19] for a SGWB necessarily requires two or more GW detectors. Such searches have been performed using two resonant-bar detectors [20] and also using two or more kilometer-scale GW interferometers (IFOs) [21–23]. The present work describes the results of the first cross-correlation analysis carried out between an IFO [the 4 km IFO at the LIGO Livingston Observatory (LLO), known as L1] and a bar (the cryogenic ALLEGRO detector, referred to as A1). This pair of detectors is separated by only 40 km, the closest pair among modern ground-based GW detector sites, which allows it to probe the stochastic GW spectrum around 900 Hz. In addition, the ALLEGRO bar can be rotated, changing the response of the correlated data streams to stochastic GWs and thus providing a means to distinguish correlations due to a SGWB from those due to correlated environmental noise [24]. This paper describes cross-correlation analysis of L1 and A1 data taken between

February 22 and March 23, 2005, during LIGO's fourth science run (S4). Average sensitivities of L1 and A1 during S4 are shown in Fig. 1. ALLEGRO was operated in three orientations, which modulated the GW response of the LLO-ALLEGRO pair through 180° of phase.

The LLO-ALLEGRO correlation experiment is complementary to experiments using data from the two LIGO sites, in that it is sensitive to a SGWB at frequencies of around 900 Hz rather than 100 Hz. Targeted sources are thus those with a relatively narrow-band spectrum peaked near 900 Hz. Spectra with such shapes can arise from

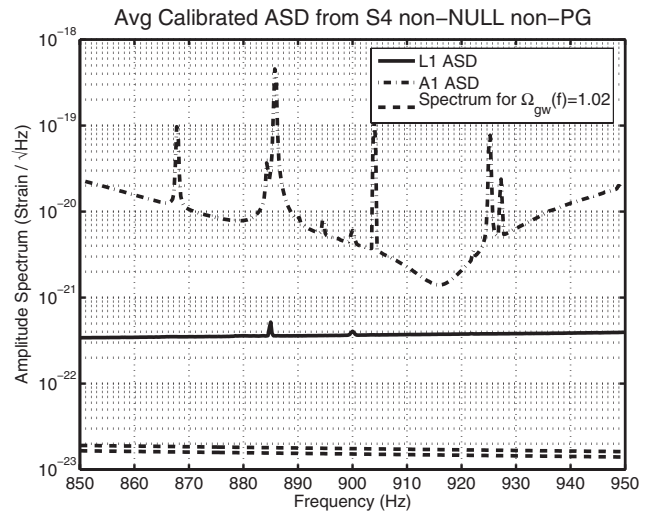


FIG. 1. Sensitivity of the LLO IFO (L1) and the ALLEGRO bar (A1) during S4, along with strain associated with $\Omega_{\text{gw}}(f) = 1.02$ (assuming a Hubble constant of $H_0 = 72 \text{ km/s/Mpc}$). [There are two $\Omega_{\text{gw}}(f) = 1.02$ curves, corresponding to the different strain levels such a background would generate in an IFO and a bar, as explained in Sec. II and [26].] The quantity plotted is amplitude spectral density (ASD), the square root of the one-sided power spectral density defined in (4.2), at a resolution of 0.25 Hz.

*Member of ALLEGRO Collaboration.

†Member of LIGO Scientific Collaboration and ALLEGRO Collaboration.

‡<http://www.ligo.org/>

exotic cosmological models, as described in Sec. II, or from astrophysical populations [16].

The organization of this paper is as follows. Section II reviews the properties and characterization of a SGWB. Section III describes the LLO and ALLEGRO experimental arrangements, including the data acquisition and strain calibration for each instrument. Section IV describes the cross-correlation method and its application to the present situation. Section V describes the details of the postprocessing methods and statistical interpretation of the cross-correlation results. Section VI describes the results of the cross-correlation measurement and the corresponding upper limit on the SGWB strength in the range 850–950 Hz. Section VII describes the results of our analysis pipeline when applied to simulated signals injected both within the analysis software and in the hardware of the instruments themselves. Section VIII compares our results to those of previous experiments and to the sensitivities of other operating detector pairs. Section IX considers the prospects for future work.

II. STOCHASTIC GRAVITATIONAL-WAVE BACKGROUNDS

A gravitational wave (GW) is described by the metric tensor perturbation $h_{ab}(\vec{r}, t)$. A given GW detector, located at position \vec{r}_{det} on the Earth, will measure a GW strain which, in the long-wavelength limit, is some projection of this tensor:

$$h(t) = h_{ab}(\vec{r}_{\text{det}}, t) d^{ab}, \quad (2.1)$$

where d^{ab} is the detector response tensor, which is

$$d_{(\text{ifo})}^{ab} = \frac{1}{2}(\hat{x}^a \hat{x}^b - \hat{y}^a \hat{y}^b) \quad (2.2)$$

for an interferometer with arms parallel to the unit vectors \hat{x} and \hat{y} and

$$d_{(\text{bar})}^{ab} = \hat{u}^a \hat{u}^b \quad (2.3)$$

for a resonant bar with long axis parallel to the unit vector \hat{u} .

A stochastic GW background (SGWB) can arise from a superposition of uncorrelated cosmological or astrophysical sources. Such a background, which we assume to be isotropic, unpolarized, stationary, and Gaussian, will generate a cross correlation between the strains measured by two detectors. In terms of the continuous Fourier transform defined by $\tilde{a}(f) = \int_{-\infty}^{\infty} dt a(t) \exp(-i2\pi ft)$, the expected cross correlation is

$$\langle \tilde{h}_1^*(f) \tilde{h}_2(f') \rangle = \frac{1}{2} \delta(f - f') S_{\text{gw}}(f) \gamma_{12}(f), \quad (2.4)$$

where

$$\gamma_{12}(f) = d_{1ab} d_{2cd} \frac{5}{4\pi} \iint d^2\Omega_{\hat{n}} P^{\text{TT}\hat{n}ab}_{cd} e^{i2\pi f \hat{n} \cdot (\vec{r}_2 - \vec{r}_1)/c} \quad (2.5)$$

is the overlap reduction function (ORF) [25] between the two detectors, defined in terms of the projector $P^{\text{TT}\hat{n}ab}_{cd}$ onto traceless symmetric tensors transverse to the unit vector \hat{n} . The ORF for several detector pairs of interest is shown in Fig. 2.

$S_{\text{gw}}(f)$ is the one-sided spectrum of the SGWB. This is the one-sided power spectral density (PSD) the background would generate in an interferometer with perpendicular arms, which can be seen from (2.4) and the fact that the ORF of such an interferometer with itself is unity. Since the ORF of a resonant bar with itself is 4/3 (see [26] and Sec. VII A for more details), the PSD of the strain measured by a bar detector due to the SGWB would be $(4/3)S_{\text{gw}}(f)$.

A related measure of the spectrum is the dimensionless quantity $\Omega_{\text{gw}}(f)$, the GW energy density per unit logarithmic frequency divided by the critical energy density ρ_c needed to close the universe:

$$\Omega_{\text{gw}}(f) = \frac{f}{\rho_c} \frac{d\rho_{\text{gw}}}{df} = \frac{10\pi^2}{3H_0^2} f^3 S_{\text{gw}}(f). \quad (2.6)$$

Note that the definition $\Omega_{\text{gw}}(f)$ thus depends on the value

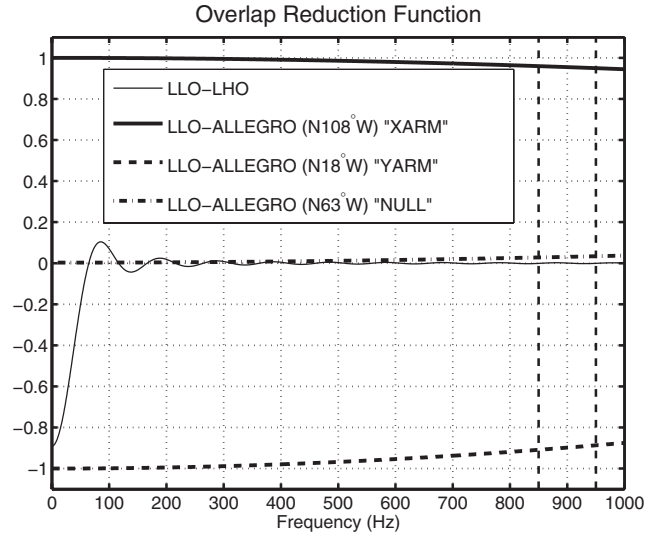


FIG. 2. The overlap reduction function for LIGO Livingston Observatory (LLO) with ALLEGRO and with LIGO Hanford Observatory (LHO). The three LLO-ALLEGRO curves correspond to the three orientations in which ALLEGRO was operated during LIGO's S4 run: “XARM” (N108°W) is nearly parallel to the x -arm of LLO (“aligned”); “YARM” (N18°W) is nearly parallel to the y -arm of LLO (“antialigned”); NULL (N63°W) is halfway in between these two orientations (a “null alignment” midway between the two LLO arms). Note that for nonzero frequencies, the separation vector between the two sites breaks the symmetry between the XARM and YARM alignments, and leads to an offset of the NULL curve, as described in [26]. The LLO-LHO overlap reduction function is shown for reference. The frequency band of the present analysis, 850 Hz $\leq f \leq$ 950 Hz, is indicated with dashed vertical lines.

of the Hubble constant H_0 . Most SGWB literature avoids this artificial uncertainty by working in terms of

$$h_{100}^2 \Omega_{\text{gw}}(f) = \left(\frac{H_0}{100 \text{ km/s/Mpc}} \right)^2 \Omega_{\text{gw}}(f) \quad (2.7)$$

rather than $\Omega_{\text{gw}}(f)$ itself. We will instead follow the precedent set by [22] and quote numerical values for $\Omega_{\text{gw}}(f)$ assuming a Hubble constant of 72 km/s/Mpc.

A variety of spectral shapes have been proposed for Ω_{gw} , for both astrophysical and cosmological stochastic backgrounds [3,27,28]. For example, whereas the slow-roll inflationary model predicts a constant $\Omega_{\text{gw}}(f)$ in the bands of LIGO or ALLEGRO, certain alternative cosmological models predict broken-power-law spectra, where the rising and falling slopes and the peak frequency are determined by model parameters [3]. String-inspired pre-big-bang cosmological models belong to this category [5,29]. For certain ranges of these three parameters, the LLO-ALLEGRO correlation measurement offers the best constraints on theory that can be inferred from any contemporary observation. This can happen, e.g., if the power-law exponent on the rising spectral slope is greater than 3 and the peak frequency is sufficiently close to 900 Hz [30].

III. EXPERIMENTAL SETUP

A. The LIGO Livingston interferometer

The experimental setup of the LIGO observatories has been described at length elsewhere [31]. Here we provide a brief review, with particular attention paid to details significant for the LLO-ALLEGRO cross-correlation measurement.

The LIGO Livingston Observatory (LLO) is an interferometric GW detector with perpendicular 4-km arms. The laser interferometer senses directly any changes in the differential arm length. It does this by splitting a light beam at the vertex, sending the separate beams into 4-km long optical cavities of their respective arms, and then recombining the beams to detect any change in the optical phase difference between the arms, which is equivalent to a difference in light travel time. This provides a measurement of $h(t)$ as defined in (2.1) and (2.2). However, the measured quantity is not exactly $h(t)$ for two reasons.

First, there are local forces which perturb the test masses, and so produce changes in arm length. There are also optical and electronic fluctuations that mimic real strains. The combination of these effects causes a strain noise $n(t)$ to always be present in the output, producing a measurement of

$$s(t) = h(t) + n(t). \quad (3.1)$$

Second, the test masses are not really free. There is a servo system, which uses changes in the differential arm length as its error signal $q(t)$, and then applies extra (“control”) forces to the test masses to keep the differential arm

length nearly zero. It is this error signal $q(t)$ which is recorded, and its relationship to the strain estimate $s(t)$ is most easily described in the Fourier domain:

$$\tilde{s}(f) = \tilde{R}(f) \tilde{q}(f). \quad (3.2)$$

The response function $\tilde{R}(f)$ is estimated by a combination of modeling and measurement [32] and varies slowly over the course of the experiment.

Because the error signal $q(t)$ has a smaller dynamic range than the reconstructed strain $s(t)$, our analysis starts from the digitized time series $q[k] = q(t_k)$ (sampled $2^{14} = 16384$ times per second, and digitally downsampled to 4096 Hz in the analysis) and reconstructs the LLO strain only in the frequency domain.

B. The ALLEGRO resonant-bar detector

The ALLEGRO resonant detector, operated by a group from Louisiana State University [33], is a two-ton aluminum cylinder coupled to a niobium secondary resonator. The secondary resonator is part of an inductive transducer [34] which is coupled to a DC SQUID. Strain along the cylindrical axis excites the first longitudinal vibrational mode of the bar. The transducer is tuned for sensitivity to this mechanical mode. Raw data acquired from the detector thus reflect the high- Q resonant mechanical response of the system. A major technical challenge of this analysis is due to the extent to which the bar data differ from those of the interferometer.

1. Data acquisition, heterodyning, and sampling

The ALLEGRO detector has a relatively narrow sensitive band of ~ 100 Hz centered around ~ 900 Hz near the two normal modes of the mechanical bar-resonator system. For this reason, the output of the detector can first be heterodyned with a commercial lock-in amplifier to greatly reduce the sampling rate, which is set at 250 samples/s. Both the in-phase and quadrature outputs of the lock-in are recorded and the detector output can thus be represented as a complex time series which covers a 250 Hz band centered on the lock-in reference oscillator frequency. This reference frequency is chosen to be near the center of the sensitive band, and during the S4 run it was set to 904 Hz. The overall timing of data heterodyned in this fashion is provided by both the sampling clock and the reference oscillator. Both time bases were locked to the Global Positioning System (GPS) time reference.

The nature of the resonant detector and its data acquisition system gives rise to a number of timing issues: heterodyning, filter delays of the electronics, and the timing of the data acquisition system itself [35]. It is of critical importance that the timing be fully understood so that the phase of any potential signal may be recovered. Convincing evidence that all of the issues are accounted for is demonstrated by the recovery and cross correlation of test signals simultaneously injected into both detectors.

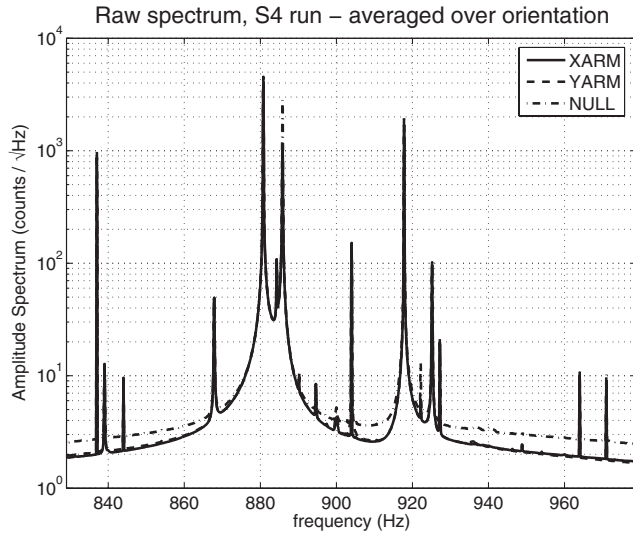


FIG. 3. The graph displays the amplitude spectral density of raw ALLEGRO detector output during S4, at a frequency resolution of 0.1 Hz. For this graph these data have not been transformed to strain via the calibrated response function. The vertical scale represents digital counts/ $\sqrt{\text{Hz}}$. The normal mechanical modes where the detector is most sensitive are at 880.78 Hz and 917.81 Hz. There is an injected calibration line at 837 Hz. Also prominent are an extra mechanical resonance at 885.8 Hz and a peak at 904 Hz (DC in the heterodyned data stream).

The signals were recovered at the expected phase as presented in Sec. VII.

2. Strain calibration

The raw detector output is proportional to the displacement of the secondary resonator, and thus has a spectrum with sharp line features due to the high- Q resonances of the bar-resonator system as can be seen in Fig. 3. The desired GW signal is the effective strain on the bar, and recovering this means undoing the resonant response of the detector. This response has a long coherence time—thus long stretches of data are needed to resolve the narrow lines in the raw data. The strain data have a much flatter spectrum, as shown in Fig. 1. Therefore it is practical to generate the

calibrated strain time series, $s(t)$, and use that as the input to the cross-correlation analysis.

The calibration procedure, described in detail in [35], is carried out in the frequency domain and consists of the following: A 30 min stretch of clean ALLEGRO data is windowed and Fourier transformed. The mechanical mode frequencies drift slightly due to small temperature variations, so these frequencies are determined for each stretch and those are incorporated into the model of the mechanical response of the system to a strain. The model consists of two double poles at these normal mode frequencies. In addition to this response, we must then account for the phase shifts due to the time delays in the lock-in and antialiasing filters.

After applying the full response function, the data are then inverse Fourier transformed back to the time domain. The next 50% overlapping 30 min segment is then taken. The windowed segments are stitched together until the entire continuous stretch of good data is completed. The first and last 15 minutes are dropped. The result represents a heterodyned complex time series of strain, whose amplitude spectral density is shown in Fig. 1.

The overall scale of the detector output in terms of strain is determined by applying a known signal to the bar. A force applied to one end of the bar has a simple theoretical relationship to an equivalent gravitational strain [35–37]. A calibrated force can be applied via a capacitive “force generator” which also provides the mechanism used for hardware signal injections. A reciprocal measurement—excitation followed by measurement with the same transducer—along with known properties of the mechanical system, allows the determination of the force generator constant. With that constant determined (with units of newtons per volt), a calibrated force is applied to the bar and the overall scale of the response determined.

3. Orientation

A unique feature of this experiment is the ability to rotate the ALLEGRO detector and modulate the response of the ALLEGRO-LLO pair to a GW background [24]. Data were taken in three different orientations of ALLEGRO, known as XARM, YARM, and NULL, detailed in Table I. As shown in Fig. 2 and (2.4), these

TABLE I. Orientations of ALLEGRO during the LIGO S4 Run, including overlap reduction function evaluated at the extremes of the analyzed frequency range, and at the frequency of peak sensitivity. Note that, while the NULL orientation represents perfect misalignment ($\gamma = 0$) at 0 Hz, it is not quite perfect at the frequencies of interest. This is primarily because of an azimuth-independent offset term in $\gamma(f)$ which contributes at nonzero frequencies [24,26]. Because of this term, it is impossible to orient ALLEGRO so that $\gamma(f) = 0$ at all frequencies, and to set it to zero around 915 Hz one would have to use an azimuth of N62°W rather than N63°W. This subtlety was not incorporated into the choice of orientations in S4, but the approximate cancellation is adequate for our purposes.

Dates	Orientation	Azimuth	$\gamma(850 \text{ Hz})$	$\gamma(915 \text{ Hz})$	$\gamma(950 \text{ Hz})$
2005 Feb 22–2005 Mar 4	YARM	N108°W	−0.9087	−0.8947	−0.8867
2005 Mar 4–2005 Mar 18	XARM	N18°W	0.9596	0.9533	0.9498
2005 Mar 18–2005 Mar 23	NULL	N63°W	0.0280	0.0318	0.0340

orientations correspond to different pair responses due to different overlap reduction functions. In the XARM orientation—the bar axis parallel to the x-arm of the interferometer—a GW signal produces positive correlation between the data in the two detectors. In the YARM orientation a GW signal produces an anticorrelation. In the NULL orientation—the bar aligned halfway between the two arms of the interferometer—the pair has very nearly zero sensitivity as a GW signal produces almost zero correlation between the detectors' data. A real signal is thus modulated whereas many types of instrumental correlation would not have the same dependence on orientation.

IV. CROSS-CORRELATION METHOD

This section describes the method to used to search for a SGWB by cross-correlating detector outputs. In the case of L1-A1 correlation measurements, it is complicated by the different sampling rates for the two instruments and the fact that the A1 data are heterodyned at 904 Hz prior to digitization.

A. Continuous-time idealization

Both ground-based interferometric and resonant-mass detectors produce a time-series output which can be related to a discrete sampling of the signal

$$s_i(t) = h_i(t) + n_i(t), \quad (4.1)$$

where i labels the detector (1 or 2 in this case), $h_i(t)$ is the gravitational-wave strain defined in (2.1), and $n_i(t)$ is the instrumental noise associated with each detector, converted into an equivalent strain. The detector output is characterized by its power spectral density $P_i(f)$,

$$\langle \tilde{s}_i^*(f) \tilde{s}_i(f') \rangle = \frac{1}{2} \delta(f - f') P_i(f), \quad (4.2)$$

which should be dominated by the autocorrelation of the noise [$\langle \tilde{s}_i^*(f) \tilde{s}_i(f') \rangle \approx \langle \tilde{n}_i^*(f) \tilde{n}_i(f') \rangle$]. If the instrument noise is approximately uncorrelated, the expected cross correlation of the detector outputs is [cf. (2.4)]

$$\langle \tilde{s}_1^*(f) \tilde{s}_2(f') \rangle \approx \langle \tilde{h}_1^*(f) \tilde{h}_2(f') \rangle = \frac{1}{2} \delta(f - f') S_{\text{gw}}(f) \gamma_{12}(f) \quad (4.3)$$

which can be used along with the autocorrelation (4.2) to determine the statistical properties of the cross-correlation statistic defined below.

We use the optimally filtered cross-correlation method described in [19,21] to calculate a cross-correlation statistic which is an approximation to the continuous-time cross-correlation statistic

$$\begin{aligned} Y^c &= \int dt_1 dt_2 s_1(t_1) Q(t_1 - t_2) s_2(t_2) \\ &= \int df \tilde{s}_1^*(f) \tilde{Q}(f) \tilde{s}_2(f). \end{aligned} \quad (4.4)$$

In the continuous-time idealization, such a cross-correlation statistic, calculated over a time T , has an expected mean

$$\mu_{Y^c} = \langle Y^c \rangle \approx \frac{T}{2} \int_{-\infty}^{\infty} df \gamma(|f|) S_{\text{gw}}(f) \tilde{Q}(f) \quad (4.5)$$

and variance

$$\sigma_{Y^c}^2 = \langle (Y^c - \mu_{Y^c})^2 \rangle \approx \frac{T}{4} \int_{-\infty}^{\infty} df P_1(f) P_2(f) |\tilde{Q}(f)|^2. \quad (4.6)$$

Using (4.5) and (4.6), the optimal choice for the filter $\tilde{Q}(f)$, given a predicted shape for the spectrum $S_{\text{gw}}(f)$ can be shown [19] to be

$$\tilde{Q}(f) \propto \frac{\gamma(|f|) S_{\text{gw}}(f)}{P_1(f) P_2(f)}. \quad (4.7)$$

If the spectrum of gravitational waves is assumed to be a power law over the frequency band of interest, a convenient parametrization of the spectrum, in terms of $\Omega_{\text{gw}}(f)$ defined in (2.6), is

$$\Omega_{\text{gw}}(f) = \Omega_R \left(\frac{f}{f_R} \right)^\alpha, \quad (4.8)$$

where f_R is a conveniently chosen reference frequency and $\Omega_R = \Omega_{\text{gw}}(f_R)$. The cross-correlation measurement is then a measurement of Ω_R , and if the optimal filter is normalized according to

$$\tilde{Q}(f) = \mathcal{N} \frac{\gamma(f) (f/f_R)^\alpha}{|f|^3 P_1(f) P_2(f)}, \quad (4.9a)$$

where

$$\mathcal{N} = \frac{20\pi^2}{3H_0^2} \left(\int_{-\infty}^{\infty} \frac{df}{f^6} \frac{[\gamma(f) (f/f_R)^\alpha]^2}{P_1(f) P_2(f)} \right)^{-1}, \quad (4.9b)$$

then the expected statistics of Y^c in the presence of a background of actual strength Ω_R are

$$\mu_{Y^c} = \Omega_R T \quad (4.10)$$

and

$$\sigma_{Y^c}^2 = T \left(\frac{10\pi^2}{3H_0^2} \right)^2 \left(\int_{-\infty}^{\infty} \frac{df}{f^6} \frac{[\gamma(f) (f/f_R)^\alpha]^2}{P_1(f) P_2(f)} \right)^{-1} \quad (4.11)$$

and a measurement of Y^c/T provides a *point estimate* of the background strength Ω_R with associated estimated error bar σ_{Y^c}/T .

B. Discrete-time method

1. Handling of different sampling rates and heterodyning

Stochastic-background measurements using pairs of LIGO interferometers [21] have implemented (4.4) from discrete samplings $s_i[k] = s(t_0 + k\delta t)$ as follows: First the continuous Fourier transforms $\tilde{s}(f)$ were approximated

using the discrete Fourier transforms of windowed and zero-padded versions of the discrete time series; then an optimal filter was constructed using an approximation to (4.7), and finally the product of the three was summed bin-by-bin to approximate the integral over frequencies. The discrete version of $\tilde{Q}(f)$ was simplified in two ways: first, because of the averaging used in calculating the power spectrum, the frequency resolution on the optimal filter was generally coarser than that associated with the discrete Fourier transforms of the data streams, and second, the value of the optimal filter was arbitrarily set to zero outside some desired range of frequencies $f_{\min} \leq f \leq f_{\max}$. This was justified because the optimal filter tended to have little support for frequencies outside that range.

The present experiment has two additional complications associated with the discretization of the time-series data. First, the A1 data are not a simple time sampling of the gravitational-wave strain, but are base banded with a heterodyning frequency $f_2^h = 904$ Hz as described in Sec. IIIB 1 and IIIB 2. Second, the A1 data are sampled at $(\delta t_2)^{-1} = 250$ Hz, while the L1 data are sampled at 16384 Hz, and subsequently downsampled to $(\delta t_1)^{-1} = 4096$ Hz. This would make a time domain cross correlation extremely problematic, as it would necessitate a large variety of time offsets $t_1 - t_2$. In the frequency domain, it means that the downsampled L1 data, once calibrated, represent frequencies ranging from -2048 Hz to 2048 Hz, while the calibrated A1 data represent frequencies ranging from $(904 - 125)$ Hz = 779 Hz to $(904 + 125)$ Hz = 1029 Hz. These different frequency ranges do not pose a problem, as long as the range of frequencies chosen for the integral satisfies $f_{\min} > 779$ Hz and $f_{\max} < 1029$ Hz. Another requirement is that, for the chosen frequency resolution, the A1 data heterodyne reference frequency must align with a frequency bin in the L1 data. This is satisfied for integer-second data spans and integer-hertz reference frequencies. With these conditions, the Fourier transforms of the A1 and L1 data are both defined over a common set of frequencies, as detailed in [38]. Looking at the A1 spectrum in Fig. 1, a reasonable range of frequencies should be a subset of the range 850 Hz $\lesssim f \lesssim 950$ Hz.

2. Discrete-time cross correlation

Explicitly, the time series inputs to the analysis pipeline, from each $T = 60$ sec of analyzed data, are:

- (i) For L1, a real time series $\{q_1[j] | j = 0, \dots, N_1 - 1\}$, sampled at $(\delta t_1)^{-1} = 4096$ Hz, consisting of $N_1 = T/\delta t_1 = 245\,760$ points. This is obtained by down-sampling the raw data stream by a factor of 4. The data are downsampled to 4096 Hz rather than 2048 Hz to ensure that the roll-off of the associated antialiasing filter is outside the frequency range being analyzed. The raw L1 data are related to gravitational-wave strain by the calibration response

- function $\tilde{R}_1(f)$ constructed as described in Sec. III A.
- (ii) For A1, a complex time series $\{s_2^h[k] | k = 0, \dots, N_2 - 1\}$, sampled at $(\delta t_2)^{-1} = 250$ Hz, consisting of $N_2 = T/\delta t_2 = 150\,000$ points. This is calibrated to represent strain data as described in Sec. IIIB 2, but still heterodyned.

To produce an approximation of the Fourier transform of the data from detector i , the data are multiplied by an appropriate windowing function, zero padded to twice their original length, discrete-Fourier-transformed, and multiplied by δt_i . In addition, the L1 data are multiplied by a calibration response function, while the A1 data are interpreted as representing frequencies appropriate in light of the heterodyne. For L1,

$$\begin{aligned} \tilde{s}_1(f_\ell) \sim \tilde{s}_1[\ell] &:= \tilde{R}_1(f_\ell) \sum_{j=0}^{N_1-1} w_1[j] q_1[j] \\ &\times \exp\left(\frac{-i2\pi\ell j}{2N_1}\right) \delta t_1, \\ \ell &= -N_1, \dots, N_1 - 1, \end{aligned} \quad (4.12)$$

where $f_\ell = \frac{\ell}{2T}$ is the frequency associated with the ℓ th frequency bin. In the case of A1, the identification is offset by $\ell_2^h = f_h \cdot (2T) = 107\,880$:

$$\begin{aligned} \tilde{s}_2(f_\ell) \sim \tilde{s}_2[\ell] &:= \sum_{k=0}^{N_2-1} w_2[k] q_2[k] \\ &\times \exp\left(\frac{-i2\pi(\ell - \ell_2^h)k}{2N_2}\right) \delta t_2, \\ \ell &= \ell_2^h - N_2, \dots, \ell_2^h + N_2 - 1. \end{aligned} \quad (4.13)$$

As is shown in [38], if we construct a cross-correlation statistic

$$Y := \sum_{\ell=\ell_{\min}}^{\ell_{\max}} \frac{1}{2T} [\tilde{s}_1(f_\ell)]^* \tilde{Q}(f_\ell) \tilde{s}_2(f_\ell), \quad (4.14)$$

the expected mean value in the presence of a stochastic background with spectrum $S_{\text{gw}}(f)$ is

$$\mu := \langle Y \rangle \approx \overline{w_1 w_2} \frac{T}{2} \sum_{\ell=\ell_{\min}}^{\ell_{\max}} \frac{1}{2T} [\tilde{Q}(f_\ell)] \gamma(f_\ell) S_{\text{gw}}(f_\ell), \quad (4.15)$$

where $\overline{w_1 w_2}$ is an average of the product of the two windows, calculated using the points which exist at both sampling rates; specifically, if r_1 and r_2 are the smallest integers such that $\delta t_1/\delta t_2 = r_1/r_2 = 125/2048$,

$$\overline{w_1 w_2} = \frac{r_1 r_2}{N} \sum_{n=0}^{N/(r_1 r_2)-1} w_1[nr_2] w_2[nr_1]. \quad (4.16)$$

Note that, while the average value given by (4.15) is manifestly real, any particular measurement of Y will be

complex, because of the bandpass associated with the heterodyning of the A1 data. As shown in [38], the real and imaginary parts of the cross-correlation statistic each have expected variance

$$\sigma^2 := \frac{1}{2} \langle Y^* Y \rangle \approx \frac{T}{8} \overline{w_1^2 w_2^2} \sum_{\ell=\ell_{\min}}^{\ell_{\max}} \frac{1}{2T} |\tilde{Q}(f_\ell)|^2 P_1(|f_\ell|) P_2(|f_\ell|), \quad (4.17)$$

where once again $\overline{w_1^2 w_2^2}$ is an average over the time samples the two windows have “in common”:

$$\overline{w_1^2 w_2^2} = \frac{r_1 r_2}{N} \sum_{n=0}^{N/(r_1 r_2)-1} (w_1[nr_2])^2 (w_2[nr_1])^2. \quad (4.18)$$

3. Construction of the optimal filter

To perform the cross correlation in (4.14), we need to construct an optimal filter by a discrete approximation to (4.9). We approximate the power spectra $P_1(f)$ using Welch’s method [39]; as a consequence of the averaging of periodograms constructed from shorter stretches of data, the power spectra are estimated with a frequency resolution δf which is coarser than the $1/2T$ associated with the construction in (4.14). As detailed in [21], we handle this by first multiplying together $[\tilde{s}_1(f_\ell)]^*$ and $\tilde{s}_2(f_\ell)$ at the finer frequency resolution, then summing together sets of $2T \delta f$ bins and multiplying them by the coarser-grained optimal filter. For our search, $\delta f = 0.25$ Hz and $T = 60$ sec, so $2T \delta f = 30$.

4. Power spectrum estimation

Because the noise power spectrum of the LLO can vary with time, we continuously update the optimal filter used in the cross-correlation measurement. However, using an optimal filter constructed from power spectra calculated from the same data to be analyzed leads to a bias in the cross-correlation statistic Y , as detailed in [40]. To avoid this, we analyze each $T = 60$ sec segment of data using an optimal filter constructed from the average of the power spectra from the segments before and after the segment to be analyzed. This method is known as “sliding power spectrum estimation” because, as we analyze successive segments of data, the segments used to calculate the PSDs for the optimal filter slide through the data to remain adjacent. The $\delta f = 0.25$ Hz resolution is obtained by calculating the power spectra using Welch’s method with 29 overlapped 4-second subsegments in each 60-second segment of data, for a total of 58 subsegments.

V. POSTPROCESSING TECHNIQUES

A. Stationarity cut

The sliding power spectrum estimation method described in Sec. IV B 4 can lead to inaccurate results if the noise level of one or both instruments varies widely over successive intervals. Most problematically, if the data are noisy only within a single analysis segment, consideration of the power spectrum constructed from the segments before and after, which are not noisy, will cause the segment to be overweighted when combining cross-correlation data from different segments. To avoid this, we calculate for each segment both the usual estimated standard deviation σ_I using the “sliding” PSD estimator and the “naive” estimated standard deviation σ'_I using the data from the segment itself. If the ratio of these two is too far from unity, the segment is omitted from the cross-correlation analysis. The threshold used for this analysis was 20%. The amount of data excluded based on this cut was between 1% and 2% in each of the three orientations, and subsequent investigations show the final results would not change significantly for any reasonable choice of threshold.

B. Bias correction of estimated error bars

Although use of the sliding power spectrum estimator removes any bias from the optimally filtered cross-correlation measurement, the methods of [40] show that there is still a slight underestimation of the estimated standard deviation associated with the finite number of periodograms averaged together in calculating the power spectrum. To correct for this, we have to scale up the error bars by a factor of $1 + 1/(N_{\text{avg}} \times 9/11)$, where N_{avg} is the number subsegments whose periodograms are averaged together in estimating the power spectrum for the optimal filter. For the data analyzed with the sliding power spectrum estimator, 29 overlapping four-second subsegments are averaged from each of two 60-second segments, for a total $N_{\text{avg}} = 58$. This gives a correction factor of $1 + 1/(58 \times 9/11) = 1.021$. The naive estimated sigmas, derived from power spectra calculated using 29 averages in a single 60-second segment, are scaled up by a factor of $1 + 1/(29 \times 9/11) = 1.042$.

C. Combination of analysis segment results

As shown in [19], the optimal way to combine a series of independent cross-correlation measurements $\{Y_I\}$ with associated one-sigma error bars is

$$Y^{\text{opt}} = \frac{\sum_I \sigma_I^{-2} Y_I}{\sum_I \sigma_I^{-2}} \quad (5.1a)$$

$$\sigma_{Y^{\text{opt}}} = \left(\sum_I \sigma_I^{-2} \right)^{-1/2}. \quad (5.1b)$$

To minimize spectral leakage, we use Hann windows in our analysis segments, which would reduce the effective observing time by approximately one-half, so we overlap the segments by 50% to make full use of as much data as possible. This introduces correlations between overlapping data segments, which modifies the optimal combination slightly, as detailed in [41].

D. Statistical interpretation

The end result of the analysis and postprocessing of a set of data is an optimally combined complex cross-correlation statistic Y^{opt} with a theoretical mean of $\Omega_R T$ and an associated standard deviation of $\sigma_{Y^{\text{opt}}}$ on both the real and imaginary parts. We can construct from this our overall point estimate on the unknown actual value of Ω_R and the corresponding one-sigma error bar:

$$\hat{\Omega}_R = Y^{\text{opt}}/T \quad (5.2a)$$

$$\sigma_\Omega = \sigma_{Y^{\text{opt}}}/T. \quad (5.2b)$$

For a given value of Ω_R , and assuming σ_Ω to be given, the likelihood function for the complex point estimate to have a particular value $\hat{\Omega}_R = x + iy$ is

$$\begin{aligned} P(x, y|\Omega_R, \sigma_\Omega) &= \frac{d^2 P}{dx dy} \\ &= \frac{1}{2\pi\sigma_\Omega^2} \exp\left(-\frac{|x + iy - \Omega_R|^2}{2\sigma_\Omega^2}\right) \\ &= \frac{1}{2\pi\sigma_\Omega^2} e^{-(x-\Omega_R)^2/2\sigma_\Omega^2} e^{-y^2/2\sigma_\Omega^2}. \end{aligned} \quad (5.3)$$

Given a prior probability density function on Ω_R , Bayes's theorem allows us to construct a posterior

$$\begin{aligned} P(\Omega_R|x, y, \sigma_\Omega) &= \frac{P(x, y|\Omega_R, \sigma_\Omega)P(\Omega_R)}{P(x, y|\sigma_\Omega)} \\ &\propto e^{-(x-\Omega_R)^2/2\sigma_\Omega^2} P(\Omega_R), \end{aligned} \quad (5.4)$$

where $x = \text{Re } \hat{\Omega}_R$. In this work we choose a uniform prior over the interval $[0, \Omega_{\text{max}}]$, where Ω_{max} is chosen to be 116 (the previous best upper limit at frequencies around 900 Hz [20]), except in the case of the hardware injections in Sec. VII C, where the *a priori* upper limit is taken to be well above the level of the injection.

Given a posterior probability density function (PDF), the 90% confidence level Bayesian upper limit Ω_{UL} is defined by

$$\int_0^{\Omega_{\text{UL}}} d\Omega_R P(\Omega_R|x, y, \sigma_\Omega) = 0.90. \quad (5.5)$$

Alternatively, any range containing 90% of the area under the posterior PDF can be thought of as a Bayesian 90% confidence level range. To allow consistent handling of results with and without simulated signals, we choose the narrowest range which represents 90% of the area under

the posterior PDF. (This is the range whose PDF values are larger than all those outside the range.) For a low enough signal-to-noise ratio $\text{Re } \hat{\Omega}_R/\sigma_\Omega$, this range is from 0 to Ω_{UL} .

E. Treatment of calibration uncertainty

In reality, the conversion of raw data from the LIGO and ALLEGRO GW detectors into GW strain is not perfect. We model this uncertainty in the calibration process as a time- and frequency-independent phase and magnitude correction, so that $\hat{\Omega}_R = x + iy$ and σ_Ω are actually related to $\Omega_R e^{\Lambda + i\phi}$, where Λ and ϕ are unknown amplitude and phase corrections; the likelihood function then becomes

$$\begin{aligned} P(x, y|\Omega_R, \sigma_\Omega, \Lambda, \phi) &= \frac{1}{2\pi\sigma_\Omega^2} \\ &\times \exp\left(-\frac{|x + iy - \Omega_R e^{\Lambda + i\phi}|^2}{2\sigma_\Omega^2}\right). \end{aligned} \quad (5.6)$$

Given a prior PDF $P(\Lambda, \phi)$ for the calibration corrections, we can marginalize over these nuisance parameters and obtain a marginalized likelihood function

$$\begin{aligned} P(x, y|\Omega_R, \sigma_\Omega) &= \int_{-\infty}^{\infty} d\Lambda \int_{-\pi}^{\pi} d\phi \\ &\times P(x, y|\Omega_R, \sigma_\Omega, \Lambda, \phi) P(\Lambda, \phi). \end{aligned} \quad (5.7)$$

We take this prior PDF to be Gaussian in Λ and ϕ , with a standard deviation added in quadrature from the quoted amplitude and phase uncertainty for the two instruments. For L1, this is 5% in amplitude and 2° in phase [32] and for A1 it is 10% in amplitude and 3° in phase [35].

VI. ANALYSIS OF COINCIDENT DATA

A. Determination of analysis parameters

To avoid biasing our results, we set aside approximately 9% of the data, spread throughout the run, as a *playground* on which to tune our analysis parameters. Based on playground investigations, we settled on the following parameters for our analysis:

- (i) Overlapping 60-second Hann-windowed analysis segments
- (ii) Frequency range $850 \text{ Hz} \leq f \leq 950 \text{ Hz}$, 0.25 Hz resolution for optimal filter
- (iii) L1 data downsampled to 4096 Hz before analysis
- (iv) Removal of the following frequencies from the optimal filter: 900 Hz (2.25 Hz wide), 904 Hz (0.25 Hz wide).

The frequencies to remove were chosen on the basis of studies of the coherence of stretches of L1 and A1 data (see Fig. 4); 900 Hz is the only harmonic of the 60 Hz power line within our analysis band, and detectable coherence is

seen for frequencies within 1 Hz of the line. 904 Hz is notched out because, as the heterodyne frequency, it corresponds to DC in the heterodyned A1 data. After completing the cross-correlation analysis, we computed the coherence from the full run of data, as shown in Fig. 5. The results are similar to those from the playground, except for a lower background level, and a feature at the heterodyning frequency.

The relevant range of frequencies can be determined by looking at the support of the integrand of (4.11), known as the *sensitivity integrand*. The overall sensitivity integrand, constructed as a weighted average over all the nonplayground data used in the analysis, is plotted in Fig. 6. The area under this curve for a range of frequencies is propor-

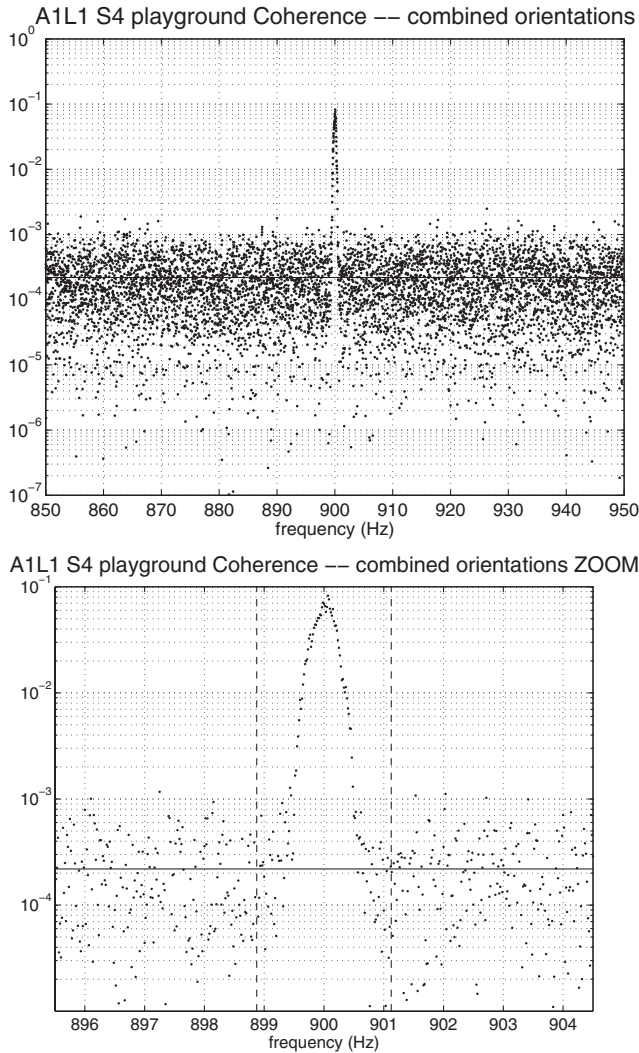


FIG. 4. LLO-ALLEGRO (L1-A1) coherence, calculated from 48.66 hours of playground data spanning nearly 30 days. The only significant feature is the power line harmonic at 900 Hz. The closeup view in the second plot shows that the coherence is insignificant beyond 1 Hz away from the line. Based on this, we mask out the nine 0.25-Hz frequency bins around 900 Hz from our analysis.

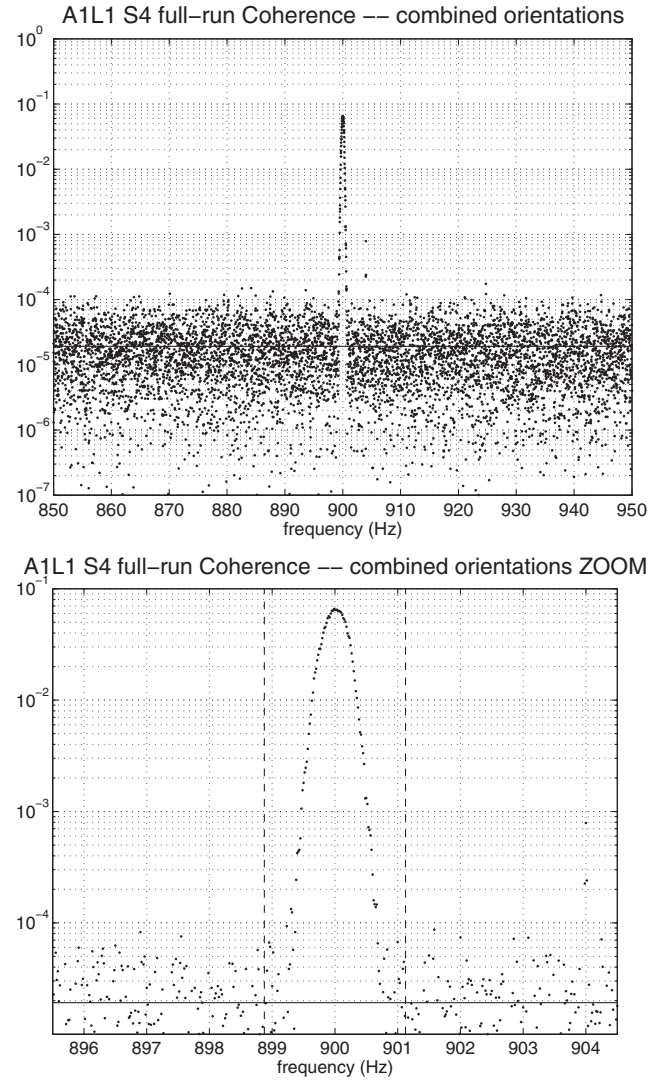


FIG. 5. LLO-ALLEGRO (L1-A1) coherence, calculated from all S4 data without regard to playground status. Again, the 900 Hz line is seen to be confined to a 2 Hz wide range. Additionally, a feature at the heterodyning frequency of 904 Hz (which was masked *a priori* in our main cross-correlation analysis) becomes visible.

tional to that frequency range's contribution to σ^{-2} . We see that the integrand does indeed become negligible by a frequency of 850 Hz on the lower end and 950 Hz on the upper end. We further see that most of the sensitivity comes from a 20-Hz wide band centered around 915 Hz.

B. Cross correlation and upper limit results

After data quality cuts, exclusion of the “playground,” and application of the stationarity cut described in Sec. VA, 44 806 one-minute segments of data were analyzed, for an effective observing time of 384.1 hours (considering the effects of Hann windowing), of which 181.2 hours was in the XARM orientation, 114.7 in the YARM orientation, and 88.2 in the NULL orientation. The

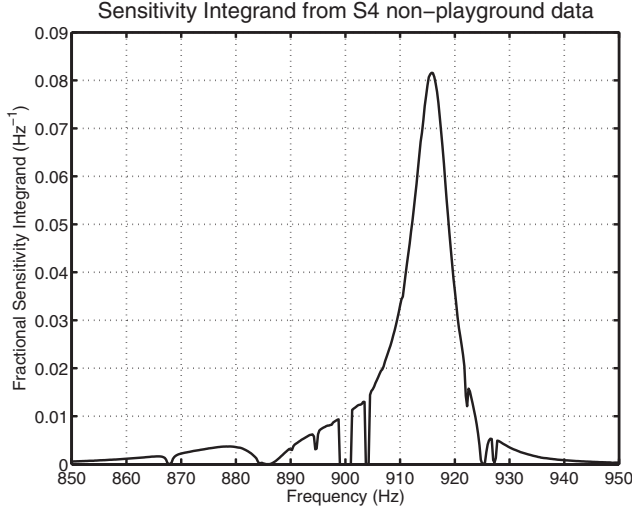


FIG. 6. The sensitivity integrand for the data used in the cross-correlation analysis, normalized so its integral equals unity. The area under this curve, between two frequencies, is the fractional contribution to σ^{-2} from that range of frequencies. Notice that the nine frequency bins masked out around 900 Hz and the one at 904 Hz give no contribution, and that the sensitivity integrand is also suppressed at other frequencies corresponding to lines in the A1 noise power spectrum.

results are shown in Table II. No statistically significant correlation is seen in any orientation, and optimal combination of all data leads to a point estimate of $0.31 + 0.30i$ for Ω_R , with a one-sigma error bar of 0.48 each on the real and imaginary parts.

The results in Table II include the ORF describing the geometry in the optimal filter. This means an orientation-independent non-GW cross correlation present in the data would change sign between XARM and YARM, and would

TABLE II. Results of optimally filtered cross correlation of nonplayground data. Results are shown for data in each of three orientations (XARM, YARM, and NULL). Additionally, the XARM and YARM results are combined with the optimal weighting (proportional to one over the square of the error bar) to give a “non-NULL” result, and results from all three orientations are optimally combined to give an overall result. In each case, T_{eff} is the effective observing time including the effects of overlapping Hann windows. Note that, since the non-NULL data are much more sensitive than the NULL data, they dominate the final result. Note also that, because the optimal filter includes the ORF, the relative orientation of LLO and ALLEGRO is already included in these results. This is reflected, for example, in the large error bars on the NULL result.

Type	T_{eff} (hrs)	Ω_R	
		Point estimate	Error bar
XARM	181.2	$0.61 + 0.25i$	0.56
YARM	114.7	$-0.47 + 0.47i$	0.90
non-NULL	295.8	$0.31 + 0.31i$	0.48
NULL	88.2	$10.96 - 43.89i$	28.62
All	384.1	$0.31 + 0.30i$	0.48

TABLE III. The cross-correlation results of Table II, scaled by $\gamma(915 \text{ Hz})$ from Table I, the value of the ORF at the frequency of peak sensitivity. This gives a sense of the “raw” cross correlation, independent of the orientation-dependent geometrical factor. The different observing times explain the remaining variation in the one-sigma error bar for the measurement, which should be inversely proportional to the square root of the observing time.

Type	T_{eff} (hrs)	$\gamma\Omega_R$	
		Point estimate	Error bar
XARM	181.2	$0.58 + 0.24i$	0.53
YARM	114.7	$0.42 - 0.42i$	0.80
NULL	88.2	$0.35 - 1.40i$	0.91

look much larger in the NULL result. One way to remove the effects of the observing geometry and compare orientation-independent cross correlations is to remove the $\gamma(f)$ from (4.9). Since the ORF for each orientation is nearly constant across the observing band, and notably across the region of peak sensitivity, it is sufficient to multiply the overall results in each case by $\gamma(915 \text{ Hz})$. This is shown in Table III, where we again see no significant cross-correlation, and sensitivities whose relative sizes are well explained by the differing observing times.

We use the methods of Secs. V D and V E to construct a posterior PDF from the overall cross-correlation measurement of $0.31 + 0.30i$ and estimated error bar of 0.48, taking into consideration the nominal calibration uncertainty of 11% in magnitude and 3.6° in phase to obtain the posterior PDF shown in Fig. 7. The narrowest 90%-likely

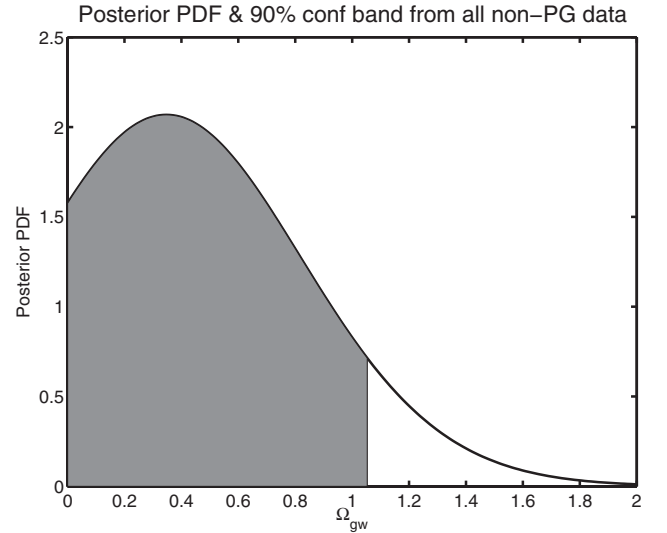


FIG. 7. Posterior probability density function associated with the overall combined point estimate of $0.31 + 0.30i$ and estimated error bar of 0.48, considering the uncertainty in the phase and amplitude of the calibration. The shaded region represents 90% of the area under the curve, leading to an upper limit on Ω_R of 1.02, which corresponds to a gravitational-wave strain of $1.5 \times 10^{-23} \text{ Hz}^{-1/2}$ at the peak frequency of 915 Hz.

confidence interval on Ω_R is $[0, 1.02]$. We thus set an upper limit of 1.02 on $\Omega_R = \Omega_{\text{gw}}(f_R)$, which translates to an upper limit on $S_{\text{gw}}(915 \text{ Hz})$ of $(1.5 \times 10^{-23} \text{ Hz}^{-1/2})^2$.

VII. VALIDATION VIA SIGNAL INJECTION

To check the effectiveness of our algorithm at detecting stochastic GW signals, we performed our search on data with simulated waveforms “injected” into them. This was done both by introducing the simulated signals into the analysis pipeline (software injections), and by physically driving both instruments in coincidence (hardware injections). Hardware injections provide an end-to-end test of our detection pipeline and also a test on the calibration accuracies of our instruments, but are necessarily short in duration because they corrupt the GW data taken during the injection. Software injections can be carried out for longer times and therefore at lower signal strengths, and can be repeated to perform statistical studies. Software injections, however, cannot check for calibration errors.

A. Signal simulation algorithm

To simulate a correlated SGWB signal in an interferometer and a bar, the formulas in, e.g., [19] need to be generalized slightly. This is because the ORF of a detector with itself is in general [26]

$$\gamma = 2[d^{ab}d_{ab} - \frac{1}{3}(d_a^a)^2], \quad (7.1)$$

which is unity for an IFO with perpendicular arms (2.2) but 4/3 for a bar (2.3). Writing this quantity for detector 1 or 2 as γ_{11} or γ_{22} , respectively, makes the required cross correlations in a simulated SGWB signal

$$\langle \tilde{h}_1^*(f) \tilde{h}_1(f') \rangle = \frac{1}{2} \delta(f - f') S_{\text{gw}}(f) \gamma_{11} \quad (7.2a)$$

$$\langle \tilde{h}_1^*(f) \tilde{h}_2(f') \rangle = \frac{1}{2} \delta(f - f') S_{\text{gw}}(f) \gamma_{12}(f) \quad (7.2b)$$

$$\langle \tilde{h}_2^*(f) \tilde{h}_2(f') \rangle = \frac{1}{2} \delta(f - f') S_{\text{gw}}(f) \gamma_{22}. \quad (7.2c)$$

The above expressions do not determine a unique algorithm for converting a set of random data streams into individual detector strains. One possible prescription is

$$\tilde{h}_1(f) = \frac{1}{2} \sqrt{S_{\text{gw}}(f)} \sqrt{\gamma_{11}} (x_1(f) + i y_1(f)) \quad (7.3a)$$

$$\begin{aligned} \tilde{h}_2(f) = & \tilde{h}_1(f) \frac{\gamma_{12}(f)}{\gamma_{11}} + \frac{1}{2} \sqrt{S_{\text{gw}}(f)} \left(\gamma_{22} - \frac{\gamma_{12}^2(f)}{\gamma_{11}} \right) \\ & \times (x_2(f) + i y_2(f)), \end{aligned} \quad (7.3b)$$

where $x_1(f)$, $y_1(f)$, $x_2(f)$, and $y_2(f)$ are statistically independent real Gaussian random variables, each of zero mean and unit variance. In the above pair, $\gamma_{12}(f)$ is used only in the construction of $\tilde{h}_2(f)$ and not of $\tilde{h}_1(f)$. A different pair, where γ_{12} is explicitly included in the calculation of both strains more symmetrically, can be defined as follows: Let $z_k(f) := (x_k(f) + i y_k(f))/\sqrt{2}$ be a pair ($k = 1, 2$) of complex random functions and let $s := \sqrt{1 - \gamma_{12}^2/(\gamma_{11}\gamma_{22})}$.

Then, the second pair can be expressed as

$$\tilde{h}_1(f) = \sqrt{\frac{S_{\text{gw}}(f)}{2}} \sqrt{\gamma_{11}} (a(f) z_1(f) + b(f) z_2(f)) \quad (7.4a)$$

$$\tilde{h}_2(f) = \sqrt{\frac{S_{\text{gw}}(f)}{2}} \sqrt{\gamma_{22}} (b(f) z_1(f) + a(f) z_2(f)), \quad (7.4b)$$

where $a = \sqrt{(1+s)/2}$ and $b = \gamma_{12}/\sqrt{2(1+s)\gamma_{11}\gamma_{22}}$ are determined completely by the three ORFs. Either pair of simulated strains obeys (7.2). The signals for software injections were generated using (7.4); those for hardware injections were generated by an older code which used (7.3). Further details of simulated signal generation are in [42].

B. Results of software simulation

We performed software injections into the full S4 coincident playground, 4316 overlapping one-minute analysis segments with an effective observing time of 37.0 hours considering the effects of Hann windows (16.7 hours of this is in the XARM orientation, 11.2 hours in the YARM orientation, and 9.0 hours in the NULL orientation). We injected constant- $\Omega_{\text{gw}}(f)$ spectra of strengths corresponding to $\Omega_R = 1.9, 3.9, 9.6$, and 19, as well as a test with the SGWB amplitude set to 0 to reproduce the analysis of the playground itself. Note that even the strongest of these injections does not produce correlations detectable in an individual one-minute analysis segment. The results are summarized in Table IV. In each case, the actual injected value of Ω_R is consistent with the real part of the point estimate to within the one-sigma estimated error bar; the imaginary part of the point estimate remains zero to within the error bar. The results for injections at $\Omega_R = 1.9$ and stronger would correspond to statistical “detections” at the 90% or better confidence level.

C. Results of hardware injection

During S4, a set of simulated signals was injected in the hardware of ALLEGRO and LLO. These injections served to test the full detection pipeline as well as the calibrations of both instruments. As described in detail in [42], the preparation of simulated waveforms for hardware injection

TABLE IV. Results of software injections. All figures are for constant- $\Omega_{\text{gw}}(f)$ and listed by Ω_R level. The 90% confidence level ranges are calculated without marginalizing over any calibration uncertainty.

Ω_R injected	Point estimate	Error bar	90% confidence interval
0	0.32 – 1.00i	1.54	[0.00, 2.74]
1.9	2.22 – 0.86i	1.55	[0.09, 4.35]
3.9	4.14 – 0.79i	1.55	[1.61, 6.66]
9.6	9.89 – 0.65i	1.56	[7.32, 12.45]
19	19.56 – 0.49i	1.58	[16.96, 22.15]

TABLE V. Results of hardware injections. Simulated waveforms with an effective signal strength of $\Omega_{\text{gw}}(f) = 8100$ were injected coincidentally in the ALLEGRO and the LIGO Livingston (LLO) detectors. The A and B sets of injections took place during the XARM and NULL observing times, respectively. Independent of the actual orientation, the simulated signals were generated and analyzed assuming different orientations: YARM, NULL, and XARM orientations were assumed for the injections labeled minus, null, and plus, respectively. The first pair of columns shows the error bars and point estimates scaled by $\gamma(915 \text{ Hz})$ to give a raw cross correlation as in Table III. (Note that, since the null alignment represents not-quite-perfect misalignment, as noted in Table I [$\gamma(915 \text{ Hz}) = 0.03$ rather than zero], the injection still leads to a statistically significant cross correlation even in the null orientation.) Note that the error bars, thus scaled, are comparable for all six injections, while the level of correlation or anticorrelation depends on the orientation associated with the injection being analyzed. The subsequent columns relate to the standard cross-correlation statistic, with the ORF included in the optimal filter, so the relative insensitivity in the null alignment is reflected in large error bars, while the point estimates are all positive and in the vicinity of the injected value of 8100. All point estimates given include corrections for known phase offsets associated with the injection system. The row labeled “all” gives the optimally weighted combination of all six results. The point estimates and one-sigma estimated error bars were combined to give 90% confidence ranges with and without marginalization over calibration uncertainty, mimicking the statistical analysis described in Secs. VD and VE.

Injection	$\gamma\Omega_R$	$\gamma\Omega_R$	Ω_R	Ω_R	Point Estimate		Unmarginalized range		Marginalized range	
	Error bar	Point estimate	Error bar	Value	Magnitude	Phase	Minimum	Maximum	Minimum	Maximum
A-minus	83	$-6623 - 126i$	93	$7403 + 141i$	7404	1.1°	7250	7555	6212	8820
A-null	99	$205 + 19i$	3106	$6429 + 607i$	6457	5.4°	1565	11 294	1435	11 562
A-plus	83	$6983 + 64i$	87	$7325 + 67i$	7325	0.5°	7182	7468	6146	8726
B-minus	95	$-6845 + 49i$	106	$7650 - 55i$	7651	-0.4°	7478	7825	6417	9115
B-null	111	$366 - 50i$	3486	$11492 - 1576i$	11 600	-7.8°	5950	17 035	5857	17 365
B-plus	92	$7128 + 77i$	96	$7477 + 80i$	7477	0.6°	7317	7634	6272	8907
All	N/A		47	$7448 + 65i$	7448	0.5°	7371	7526	6256	8867

tions requires application of the transfer function of the hardware component that is actuated, such as one of the two end test masses in LLO, to the theoretical strain for that instrument. Subsequent refinements to instrumental calibration mean that the precise injected signal strength is determined after the fact. Six hardware injections performed during S4, each 1020 seconds long, had an effective constant $\Omega_{\text{gw}}(f)$ of 8100. The series of injections we call “A” and “B” were performed during the XARM and NULL observation periods, respectively. Independent of the physical orientation of ALLEGRO, the injection and analysis was performed for three different assumed orientations, producing “plus” (aligned, as in the XARM orientation), “minus” (antialigned, as in YARM), and “null” (misaligned, as in NULL) injections in each series. The results (after correcting for known phase offsets in the injection systems) for each of the six injections are shown in Table V.

The results show some variation of magnitude and phase of the point estimates, especially for the null injections. However, all the injection results are consistent with the injected signal strength to within statistical and systematic uncertainties. This is illustrated informally in Fig. 8, which shows the point estimates on the complex plane, each surrounded by an error circle of radius 2.15 times the corresponding estimated error bar. (This radius was chosen because 90% of the volume under a two-dimensional Gaussian falls within a circle of radius 2.15σ .) Those circles all overlap with a region centered at the actual injection strength illustrating the magnitude and phase uncertainty in the calibration. The systematic error can

be more quantitatively evaluated using the method of Sec. VE to produce a posterior PDF associated with each injection measurement. This is illustrated for the optimally combined point estimate of $7448 + 65i$ and associated estimated error bar 47 in Fig. 9, and ranges corresponding to the most likely 90% confidence range under the posterior PDFs (with and without marginalization) are included in Table V. For each of the six injections, as well as for the combined result, the actual injected value of 8100 falls into the range after marginalization over the calibration uncertainty.

VIII. COMPARISON TO OTHER EXPERIMENTS

The previous most sensitive direct upper limit at the frequencies probed by this experiment was set by cross correlating the outputs of the Explorer and Nautilus resonant-bar detectors [20]. They found an upper limit on $h_{100}^2\Omega_{\text{gw}}(907.20 \text{ Hz})$ of 60. Using the value of 72 km/s/Mpc for the Hubble constant, that translates to a limit of 116 on $\Omega_{\text{gw}}(907.20 \text{ Hz})$, upon which our limit of 1.02 is a hundredfold improvement.

Data from LLO, taken during S4, were also correlated with data from the LIGO Hanford Observatory (LHO) to set an upper limit on $\Omega_{\text{gw}}(f)$ at frequencies between 50 Hz and 150 Hz [23]. Correlations between LLO and LHO are not suited to measurements at high frequencies because of the effects of the ORF, illustrated in Fig. 2. For comparison, rough measurements using S4 LLO-LHO data and a band from 850 Hz to 950 Hz yield upper limits of around 20, while those confined to $905 \text{ Hz} \leq f \leq 925 \text{ Hz}$ (the band

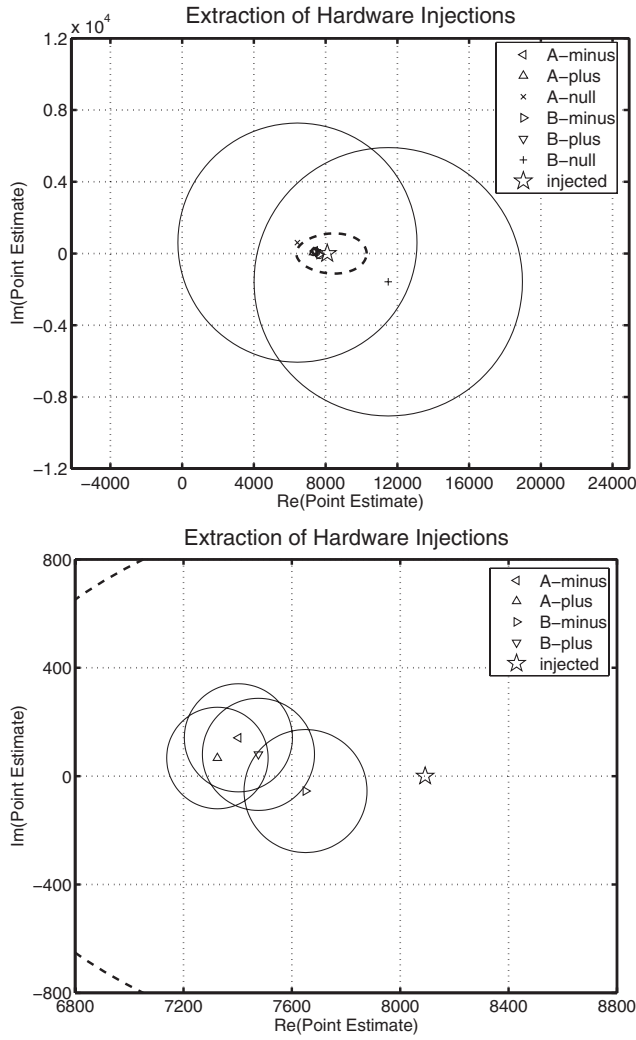


FIG. 8. Visualization of hardware injection results. Each of the six point estimates of Ω_R is plotted on the complex plane, with an associated error circle of 2.15 times the estimated one-sigma error bar. (This contains 90% of the volume under the corresponding likelihood surface.) The five-pointed star indicates the actual injected level of $\Omega_R = 8100$. The dashed teardrop-shaped region indicates the calibration uncertainty, corresponding to a 2.15-sigma ellipse in log-amplitude/phase space. On the left we see that the two null injections are consistent in amplitude and phase with the actual injection, considering the statistical uncertainty associated with the real and imaginary parts of their point estimates. The plot on the right (in which the edge of the dashed calibration uncertainty teardrop can just be seen) shows that the plus and minus injections are all statistically consistent with each other, and consistent with the injection when systematic uncertainties associated with calibration are taken into account.

contributing most of the L1-A1 sensitivity) give upper limits of around 80.

Correlations between the 4 km and 2 km IFOs at LHO, known as H1 and H2, respectively, are not suppressed by the ORF, which is identically unity for colocated, coaligned IFOs. Since H1 and L1 have comparable sensitiv-

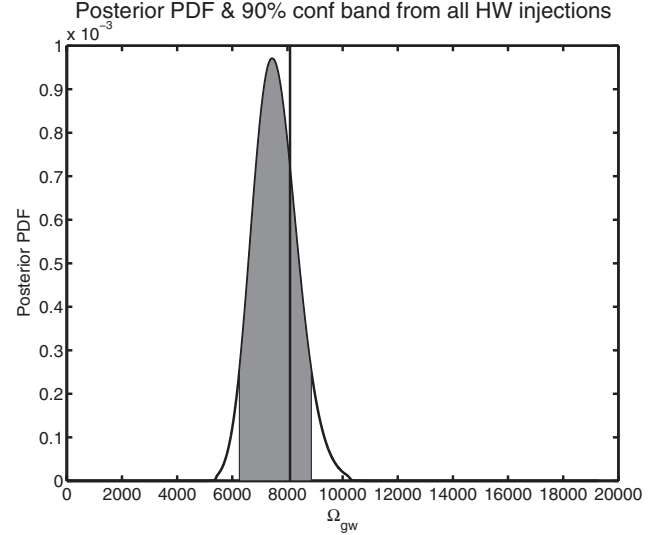


FIG. 9. Posterior probability density function associated with combined hardware injection measurement, including marginalization over calibration uncertainties. Note that, while the combined one-sigma statistical error bar is only 47, the shaded 90% area under the curve has a width of over 2000. This is because systematic errors dominate in the presence of the large point estimate. The solid vertical line indicates the actual injection level of $\Omega_R = 8100$.

ities, the most significant factor in comparing H1-H2 to L1-A1 sensitivity is the relative sensitivities of A1 and H2. Since H2 was about a factor of 50 (in power) more sensitive than A1 during S4, averaged across the band from 905 Hz to 925 Hz, we would expect an H1-H2 correlation measurement during S4 to be a factor of 7 or better more sensitive than L1-A1 as a measure of $\Omega_{\text{gw}}(f)$ at these frequencies. However, the fact that H1 and H2 share the same physical environment at LHO necessitates a careful consideration of correlated noise which is ongoing [43].

Work is also currently under way to search for a SGWB at frequencies around 900 Hz by correlating data from the Virgo IFO with the resonant-bar detectors Auriga, Explorer, and Nautilus [44].

Finally, an indirect limit can be set on SGWB strength due to the energy density in the associated gravitational waves themselves, which is given by

$$\rho_{\text{gw}} = \rho_{\text{crit}} \int_0^\infty \frac{\Omega_{\text{gw}}(f)}{f} df. \quad (8.1)$$

The most stringent limit is on a cosmological SGWB, set by the success of big-bang nucleosynthesis, is $\rho_{\text{gw}}/\rho_{\text{crit}} \leq 1.1 \times 10^{-5}$ [3]. In comparison, a background of the strength constrained by our measurement, $\Omega_R = 1.02$, would contribute about 2×10^{-2} to $\rho_{\text{gw}}/\rho_{\text{crit}}$, if it were confined to the most sensitive region between 905 Hz and 925 Hz. (Spread over the full range of integration $850 \text{ Hz} \leq f \leq 950 \text{ Hz}$, it would contribute 1×10^{-1} .)

Note, however, that this nucleosynthesis bound is not relevant for a SGWB of astrophysical origin.

IX. FUTURE PROSPECTS

LIGO's S5 science run began in November 5, 2005, with the aim of collecting 1 yr of coincident data at LIGO design sensitivity. ALLEGRO has also been in operation over that time period, so the measurement documented in this paper could be repeated with S5 data. Such a measurement would be more sensitive due to L1's roughly fivefold reduction in strain noise power at 900 Hz between S4 and S5, and because of the larger volume of data (roughly 20 times as much). Those two improvements could combine to lead to an improvement of about an order of magnitude in Ω_R sensitivity. However, no immediate plans exist to carry out an analysis with S5 data, because this incremental quantitative improvement in sensitivity would still leave us far from the level needed to detect a cosmological background consistent with the nucleosynthesis bound, or an astrophysical background arising from a realistic model.

Additionally, the greater sensitivity of the H1-H2 pair means that a background detectable with L1-A1 would first be seen in H1-H2. In the event that a "surprise" correlation is seen in H1-H2 which cannot be attributed to noise, correlation measurements such as LLO-ALLEGRO and Virgo-AURIGA could be useful for confirming or ruling out a gravitational origin.

X. CONCLUSIONS

We have reported the results of the first truly heterogeneous cross-correlation measurement to search for a stochastic gravitational-wave background. While the upper limit of $1.5 \times 10^{-23} \text{ Hz}^{-1/2}$ on the strain of the SGWB corresponds to a hundredfold improvement over the previous direct upper limit on $\Omega_{\text{gw}}(f)$ in this frequency band [20], the amplitude of conceivable spectral shapes is already constrained more strongly by results at other fre-

quencies [22,23]. The lasting legacy of this work is thus more likely the overcoming of technical challenges of cross-correlating data streams from instruments with significantly different characteristics. Most obviously, we performed a coherent analysis of data from resonant-mass and interferometric data, but additionally the data were sampled at different rates, ALLEGRO data were heterodyned and therefore complex in the time domain, and entirely different methods were used for the calibrations of both instruments. Lessons learned from this analysis will be valuable not only for possible collaborations between future generations of detectors of different types, but also between interferometers operated by different collaborations.

ACKNOWLEDGMENTS

The authors gratefully acknowledge the support of the United States National Science Foundation for the construction and operation of the LIGO Laboratory and the Particle Physics and Astronomy Research Council of the United Kingdom, the Max-Planck-Society and the State of Niedersachsen/Germany for support of the construction and operation of the GEO600 detector. The authors also gratefully acknowledge the support of the research by these agencies and by the Australian Research Council, the Natural Sciences and Engineering Research Council of Canada, the Council of Scientific and Industrial Research of India, the Department of Science and Technology of India, the Spanish Ministerio de Educacion y Ciencia, The National Aeronautics and Space Administration, the John Simon Guggenheim Foundation, the Alexander von Humboldt Foundation, the Leverhulme Trust, the David and Lucile Packard Foundation, the Research Corporation, and the Alfred P. Sloan Foundation. The ALLEGRO observatory is supported by the National Science Foundation, Grant No. PHY0215479. This paper has been assigned LIGO Document No. LIGO-P050020-09-Z.

-
- [1] N. Christensen, Phys. Rev. D **46**, 5250 (1992).
 - [2] B. Allen, in *Proceedings of the Les Houches School on Astrophysical Sources of Gravitational Waves, Les Houches, 1995*, edited by J.A. Marck and J.P. Lasota (Cambridge University Press, Cambridge, England, 1996), p. 373.
 - [3] M. Maggiore, Phys. Rep. **331**, 283 (2000).
 - [4] M. Gasperini and G. Veneziano, Astropart. Phys. **1**, 317 (1993).
 - [5] M. Gasperini and G. Veneziano, Phys. Rep. **373**, 1 (2003).
 - [6] A. Buonanno, M. Maggiore, and C. Ungarelli, Phys. Rev. D **55**, 3330 (1997).
 - [7] L.P. Grishchuk, Sov. Phys. JETP **40**, 409 (1975).
 - [8] L.P. Grishchuk, Classical Quantum Gravity **14**, 1445 (1997).
 - [9] A.A. Starobinsky, Pis'ma Zh. Eksp. Teor. Fiz. **30**, 719 (1979) [JETP Lett. **30**, 682 (1979).]
 - [10] A. Kosowsky, M.S. Turner, and R. Watkins, Phys. Rev. Lett. **69**, 2026 (1992).
 - [11] R. Apret, M. Maggiore, A. Nicolis, and A. Riotto, Nucl. Phys. **B631**, 342 (2002).
 - [12] R.R. Caldwell and B. Allen, Phys. Rev. D **45**, 3447 (1992).
 - [13] T. Damour and A. Vilenkin, Phys. Rev. Lett. **85**, 3761 (2000).
 - [14] T. Damour and A. Vilenkin, Phys. Rev. D **71**, 063510 (2005).

- (2005).
- [15] T. Regimbau and J.A. de Freitas Pacheco, *Astron. Astrophys.* **376**, 381 (2001).
 - [16] T. Regimbau and J.A. de Freitas Pacheco, *Astron. Astrophys.* **447**, 1 (2006).
 - [17] D.M. Coward, R.R. Burman, and D.G. Blair, *Mon. Not. R. Astron. Soc.* **329**, 411 (2002).
 - [18] A. Cooray, *Mon. Not. R. Astron. Soc.* **354**, 25 (2004).
 - [19] B. Allen and J.D. Romano, *Phys. Rev. D* **59**, 102001 (1999).
 - [20] P. Astone *et al.*, *Astron. Astrophys.* **351**, 811 (1999).
 - [21] B. Abbott *et al.* (LIGO Scientific Collaboration), *Phys. Rev. D* **69**, 122004 (2004).
 - [22] B. Abbott *et al.* (LIGO Scientific Collaboration), *Phys. Rev. Lett.* **95**, 221101 (2005).
 - [23] B. Abbott *et al.* (LIGO Scientific Collaboration), *Astrophys. J.* **659**, 918 (2007).
 - [24] L.S. Finn and A. Lazzarini, *Phys. Rev. D* **64**, 082002 (2001).
 - [25] É.É. Flanagan, *Phys. Rev. D* **48**, 2389 (1993).
 - [26] J.T. Whelan, *Classical Quantum Gravity* **23**, 1181 (2006).
 - [27] D.M. Coward, R.R. Burman, and D.G. Blair, *Mon. Not. R. Astron. Soc.* **324**, 1015 (2001).
 - [28] V. Ferrari, S. Matarrese, and R. Schneider, *Mon. Not. R. Astron. Soc.* **303**, 247 (1999).
 - [29] R. Brustein, M. Gasperini, M. Giovannini, and G. Veneziano, *Phys. Lett. B* **361**, 45 (1995).
 - [30] S. Bose, *Phys. Rev. D* **71**, 082001 (2005).
 - [31] B. Abbott *et al.*, *Nucl. Instrum. Methods Phys. Res., Sect. A* **517**, 154 (2004).
 - [32] A. Dietz *et al.*, LIGO Report, 2005, <http://www.ligo.caltech.edu/docs/T/T050262-00.pdf>.
 - [33] <http://gravity.phys.lsu.edu/>
 - [34] Gregory M. Harry, Ph.D. thesis, University of Maryland, 1999.
 - [35] M.P. McHugh and W.W. Johnson, LIGO Report, 2006, <http://www.ligo.caltech.edu/docs/T/T060096-01.pdf>.
 - [36] M.P. McHugh *et al.*, *Classical Quantum Gravity* **22**, S965 (2005).
 - [37] A. Morse, W.O. Hamilton, W.W. Johnson, E. Mauceli, and M.P. McHugh, *Phys. Rev. D* **59**, 062002 (1999).
 - [38] J.T. Whelan *et al.*, *Classical Quantum Gravity* **22**, S1087 (2005).
 - [39] P.D. Welch, *IEEE Trans. Audio Electroacoust.* **15**, 70 (1967).
 - [40] A. Lazzarini, LIGO Report, 2004, <http://www.ligo.caltech.edu/docs/T/T040128-02.pdf>.
 - [41] A. Lazzarini and J. Romano, LIGO Report, 2004, <http://www.ligo.caltech.edu/docs/T/T040089-00.pdf>.
 - [42] S. Bose *et al.*, *Classical Quantum Gravity* **20**, S677 (2003).
 - [43] Nickolas V. Fotopoulos (LIGO Scientific Collaboration), *Classical Quantum Gravity* **23**, S693 (2006).
 - [44] Elena Cuoco (Virgo Collaboration), presentation from the XIth Marcel Grossmann Meeting, 2006 (to be published), http://www.cascina.virgo.infn.it/vsb/slides/Cuoco_MG11.ppt.